Research Square

Preprints are preliminary reports that have not undergone peer review.
They should not be considered conclusive, used to inform clinical practice,
or referenced by the media as validated information.

Urban Morphology and Thermal Exposure in Senegal's Major Cities

Souleymane THIAM[1]

s.t2@zig.univ.sn

Assane Seck University of Ziguinchor

Samo DIATTA[1]

Assane Seck University of Ziguinchor

Research Article

Keywords: Local Climate Zones, Land Surface Temperature, Heat stress, Land Use/Land Cover, Senegal, Random Forest

Posted Date: November 9th, 2026

DOI: https://doi.org/10.21203/rs.3.rs-11406053/v1

License: This work is licensed under a Creative Commons Attribution 4.0 International License.
Read Full License

Additional Declarations: No competing interests reported.

Urban Morphology and Thermal Exposure in Senegal's Major Cities

Souleymane THIAM[1]*, Samo DIATTA[1],

[1]Laboratory of Oceanography, Environmental and Climate Sciences (LOSEC), Assane Seck University of Ziguinchor, Ziguinchor, Senegal

*Corresponding author: Souleymane THIAM (s.t2@zig.univ.sn)

Abstract

Accelerating urbanization across West Africa is intensifying urban heat islands (UHIs), yet the national-scale thermal consequences remain largely unquantified. This study presents an integrated characterization of urban morphology and thermal exposure across eight major Senegalese cities Dakar, Touba, Thiès, Kaolack, Mbour, Rufisque, Saint-Louis, and Ziguinchor over a 24-year analytical window (2000–2024). Four complementary approaches were combined: (i) a high-resolution Local Climate Zone (LCZ) classification produced with GeoClimate v1.0 from OpenStreetMap data following the Stewart and Oke (2012) standard; (ii) a multi-temporal land use/land cover (LULC) analysis (2000–2020) integrating MODIS MCD12Q1 and GHSL GHS-BUILT-S products; (iii) spatiotemporal land surface temperature (LST) retrieval from the Landsat archive processed on Google Earth Engine (GEE); and (iv) a 2024 heat-stress map using a Random Forest supervised classifier combining LST, NDVI, and NDBI (overall accuracy 98.1%, Kappa 0.936). Built-up surfaces expanded by approximately 357,000 ha over 2000–2020 (+170%), with 61.1% converted from savanna and 37.3% from agricultural land. This expansion produced a national LST increase of +1.2 °C and urban surface temperatures reaching 49.0 °C in Touba. The LCZ–heat stress cross-analysis (Kruskal–Wallis $H = 143.7$, $p < 0.001$) reveals a robust morpho-thermal gradient: compact built-up zones (LCZ 2–3) exhibit mean stress scores ($\bar{S}$) two to three times higher than those of natural zones. This gradient is further modulated by a systematic macroclimatic offset of 0.5–0.8 $\bar{S}$ units between coastal and Sahelian inland cities, irrespective of LCZ class. Building surface fraction (BSF, $\rho = 0.74$) and pervious surface fraction (PERVF, $\rho = -0.71$) emerge as the primary morphological determinants of thermal exposure. A key original finding is the LCZ A paradox: dense trees provide effective cooling in humid Ziguinchor ($\bar{S} = 1.1$) but remain thermally near-neutral in arid Touba ($\bar{S} = 2.7$), demonstrating that canopy density and soil water availability are the critical conditions governing the cooling efficacy of urban greening in dryland contexts. These findings provide the first national LCZ baseline for Senegal and an open-source methodological framework transferable to Sahelian cities across West Africa. They also constitute an operational mapping foundation for mainstreaming UHI mitigation into the revision of Senegal's Nationally Determined Contribution (NDC) and the monitoring of SDGs 11 and 13.

Keywords: Local Climate Zones · Land Surface Temperature · Heat stress· Land Use/Land Cover · Senegal · Random Forest

1. Introduction

Urbanization is the most consequential anthropogenic transformation of the twenty-first century. The United Nations projects that about 68% of the global population will live in urban areas by 2050. Sub-Saharan Africa (SSA) records the world's highest urban growth rates, exceeding 4% per year, and is expected to account for nearly 60% of global urban population growth by mid-century (UN-DESA, 2022). Senegal exemplifies this trajectory, with its urban population rising from 41% in 2000 to 49% in 2023, and projections exceeding 60% by 2030 (ANSD, 2023; World Bank, 2023). This unprecedented urban expansion reconfigures surface energy balances, hydrological cycles, and atmospheric boundary-layer dynamics, manifesting as urban heat islands (UHIs), in which built-up surfaces record significantly higher temperatures than their rural surroundings (Oke, 1982; Arnfield, 2003).

The UHI effect arises when vegetated, high-evapotranspiration surfaces are replaced by impervious materials with low albedo, high thermal capacity, and poor moisture retention (Grimmond, 2007; Akbari et al., 2016). Its consequences are wide-ranging and well documented globally: excess mortality during heat events (Laaidi et al., 2012), increased cooling energy demand (Li et al., 2019), degraded air quality, and chronic heat stress that disproportionately affects the most vulnerable urban populations (Santamouris, 2015). In Sub-Saharan Africa, where ambient temperatures already exceed thermal comfort thresholds for much of the year, UHI-driven temperature increases pose a direct public health threat, with UHI-attributable warming projected to be +2 to +4 °C under business-as-usual scenarios by 2100 (Niang et al., 2014; Ermert et al., 2023). In Senegal, preliminary studies have documented urban–rural thermal differentials of 4–5 °C in Dakar (Ndiaye et al., 2020), yet no systematic national-scale analysis integrating urban morphology, temporal dynamics, and heat stress has been conducted.

Despite these stakes, SSA cities remain severely underrepresented in global UHI research (Roth, 2007; Engström et al., 2020). Most studies in West Africa are limited to single-city analyses of Dakar, Accra, or Lagos and do not incorporate urban morphology within a comparative, multi-temporal framework (Diallo et al., 2020; Guzman-Echavarria and Ghosh, 2022). This gap is

particularly concerning because West African cities exhibit morphologies, climatic contexts, and urbanization trajectories that differ fundamentally from those of European, Asian, or North American cities, on which most UHI literature is grounded.

The Local Climate Zone (LCZ) framework, developed by Stewart and Oke (2012) and refined by Demuzere et al. (2022), offers a direct methodological response to this gap. By classifying urban and natural landscapes into 17 standardized categories defined by geometry (building height, density, and spacing), surface cover (albedo, permeability), and thermal properties (admittance, emissivity), the LCZ framework provides a physically grounded link between urban form and thermal response, independent of administrative definitions or cross-national data inconsistencies. The global WUDAPT initiative (Ching et al., 2018) has produced LCZ maps for hundreds of cities worldwide, yet West Africa remains a major geographical gap in this coverage (Kotharkar & Ramesh, 2023). Concurrently, advances in Google Earth Engine (GEE; Gorelick et al., 2017) and machine learning algorithms, notably Random Forest (Breiman, 2001), have democratized access to large-scale, multi-temporal, and multi-city analyses in institutionally data-scarce regions, enabling rigorous characterization of the morphology–climate relationship at the national scale.

The present study addresses five research questions: (1) How have built-up surfaces and land cover changed across Senegal from 2000 to 2020, and which land cover types have been converted? (2) What are the dominant LCZ types in selected Senegalese cities, and how does urban morphology vary between coastal and inland climatic contexts? (3) How has LST changed spatially and temporally from 2000 to 2020, and what is the UHI intensity at the city scale? (4) What is the spatial distribution of heat stress in 2024, and which zones are most exposed? (5) To what extent do LCZ classes predict thermal exposure, and how does this relationship vary across climatic contexts?

These findings inform operational recommendations for climate-resilient urban planning, aligned with SDGs 11 and 13 and with Senegal's Nationally Determined Contribution (NDC).

The paper is organized as follows: Sect. 2 describes the observational datasets and methodology for characterizing the LCZ classification, land cover/land use analysis, LST, and Heat stress

88 classification. Sect. 3 presents the results. The discussion of the results according to the main
89 processes is presented in Sect. 4. Finally, conclusions are summarized in Sect. 5.
90
91 ## 2. Materials and Methods
92 ### 2.1 Study Area

93 Senegal (11°30'–16°41'N; 11°21'–17°32'W) is a West African country covering 196722 km², bordered by Mauritania to the north, Mali to the east, Guinea and Guinea-Bissau to the south, and the Atlantic Ocean to the west. With an estimated 2025 population of 19 million, 55.05% of whom live in urban areas, Senegal ranks among the most rapidly urbanizing countries in Sub-Saharan Africa (ANSD, 2026). The territory spans three major bioclimatic zones, defined by a latitudinal rainfall gradient: (i) a Sahelian zone in the north (Saint-Louis, Touba), with mean annual rainfall below 400 mm and mean annual temperatures exceeding 30 °C; (ii) a Sudano-Sahelian zone in the center (Thiès, Kaolack), receiving 500–800 mm of annual rainfall; and (iii) a Sudano-Guinean zone in the south (Ziguinchor), receiving 1000–1500 mm per year. Coastal cities such as Dakar, Rufisque, Mbour, and Saint-Louis also benefit from significant thermal moderation driven by cold-water upwelling of the Canary Current along the Atlantic seaboard, which reduces peak daytime temperatures by 3–5 °C relative to inland cities (Tall et al., 2020).

105 The study encompasses the eight most populous cities in Senegal (**Fig. 1**; Table 1), namely Dakar
106 (1327422 inhabitants), Touba (1189759), Thiès (401521 inhabitants), Kaolack (313767), Mbour
107 (300899), Rufisque (306772), Saint-Louis (266278), and Ziguinchor (222879), according to
108 ANSD (2024).

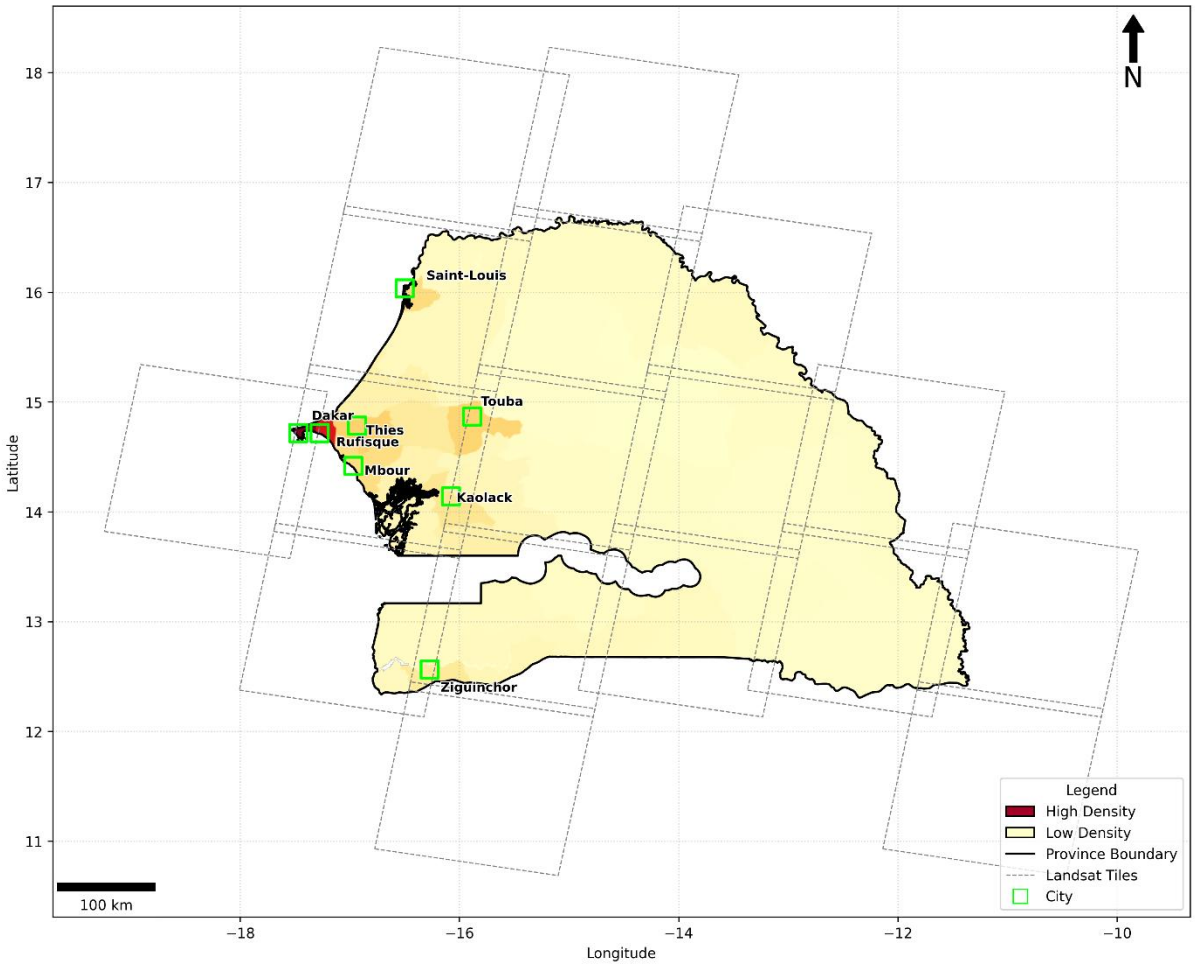


Fig. 1. Study area: Population density and location of the eight urban centers studied in Senegal, selected based on population size (GPWv4, 2020). The color gradient represents population density (dark red = high density; light yellow = low density). Landsat tiles used in the analysis are shown as dashed outlines. Source: GPWv4 (2020).

Together, these cities account for more than 75% of the national urban population and span Senegal's full bioclimatic gradient, from the Atlantic coastal domain to the Sahelian interior, encompassing a wide range of urban morphologies and socioeconomic conditions. This dual criterion of demographic weight and climatic representativeness makes them an ideal ensemble for identifying interactions among urban morphology, macroclimatic context, and thermal exposure at the national scale.

Table 1. Characteristics of the eight targeted Senegalese cities. ANSD (2024) for demographic data; Tall et al. (2020) and CHIRPS rainfall data for mean annual precipitation.

City	Population (ANSD, 2025)	Climatic zone	Mean annual rainfall (mm/yr)	Latitude	Longitude
Dakar	1 327 000	Coastal Sahelian	450–550	14.69°N	17.44°W
Touba	1 189 759	Inland Sahelian	300–450	14.86°N	15.88°W
Thies	401 521	Sudano-Sahelian	550–700	14.79°N	16.93°W
Kaolack	313 767	Sudano-Sahelian	600–800	14.15°N	16.07°W
Mbour	300 899	Coastal Sudano-Sahelian	550–700	14.37°N	16.97°W
Rufisque	306 772	Coastal Sahelian	450–550	14.71°N	17.27°W
Saint-Louis	266 278	Coastal Sahelian	250–350	16.02°N	16.50°W
Ziguinchor	222 879	Sudano-Guinean	1,000–1,500	12.56°N	16.27°W

2.2 Local Climate Zone Classification

LCZ mapping is performed using the open-source GeoClimate framework (Bocher et al., 2021; https://github.com/orbisgis/geoclimate), a geoprocessing tool that automatically derives geographical indicators characterizing the physical properties of urban territories in a reproducible manner. The LCZ framework classifies urban and natural landscapes into 17 standardized categories: 10 built-up types (LCZ 1–10) and 7 natural land cover types (LCZ A–G), defined by geometry, surface cover, and thermal properties (Stewart & Oke, 2012), as illustrated in **Fig. 2**. Built on OpenStreetMap (OSM) data, GeoClimate computes key urban morphological parameters, including building height, impervious surface fraction, and sky view factor, and assigns a primary LCZ class to each Reference Spatial Unit (RSU). We extracted OSM data for each of the eight study cities via the Overpass API and visually validated it against very high-resolution Google Earth Pro imagery. We then converted numerical codes (1–10, 101–107) to standard LCZ labels (LCZ 1 to LCZ G) using the lookup table from Demuzere et al. (2022).



Fig. 2. Typology of the 17 Local Climate Zones (LCZ) according to Stewart and Oke (2012) and WUDAPT. Classes 1 to 10 represent built-up types; classes A to G represent natural land cover types.

2.3 Land Use/Land Cover Analysis and Built-up Transition Mapping (2000–2020)

Land use/land cover (LULC) is mapped for three dates (2000, 2010, and 2020) at 100 m spatial resolution from two complementary data sources:

- **MODIS MCD12Q1 (Collection 6.1)** is a global annual land cover product at 500 m, based on the International Geosphere-Biosphere Program (IGBP) classification scheme (Friedl & Sulla-Menashe, 2022). After resampling to 100 m and reclassification, five thematic classes were retained: water, forest, savanna, agriculture, and bare soil.
- **GHSL GHS-BUILT-S (JRC, 2023):** a dedicated global built-up surface product at 100 m that provides per-pixel built-up surface fraction estimates. Pixels with a built-up fraction greater than zero were binarized to produce a built-up/non-built-up layer.

We integrated the layers by prioritizing the GHSL built-up layer and then filling the remaining classes with the MODIS classification. For each reference year, we computed national land cover areas by class and derived transition matrices for built-up land for the periods 2000–2010, 2010–2020, and 2000–2020. All processing was conducted on the Google Earth Engine (GEE) cloud computing platform, and the outputs were exported as GeoTIFF files.

Table 2. Land use/land cover classes, descriptions, and data sources.

Code	LULC Class	Description	MODIS Source (IGBP)
0	Water	Water bodies, rivers, lakes	Classes 11, 17
1	Forest	Dense and open forests	Classes 1-5
2	Rangeland	Wooded and shrub savannas	Classes 6-10
3	Agriculture	Croplands and cultivated land	Classes 12, 14
4	Bult-up	Urban areas	GHSL GHS_BUILT_S
5	Barren	Bare soil and desert	Classes 15, 16

2.4 Land Surface Temperature Retrieval for Multi-temporal Analysis (2000–2020)

We retrieved LST from the Landsat Collection 2 Level-2 archive (USGS, 2021), which includes Landsat 5 TM, Landsat 7 ETM+, and Landsat 8 TIRS, for three target periods: 2000, 2010, and 2020 (March–June dry-season peak). Images were filtered for cloud cover (<10%) and screened using the per-pixel quality assessment (QA) band mask. We derived LST from the thermal infrared bands using the single-channel algorithm of Jiménez-Muñoz et al. (2014), with a surface emissivity correction based on the NDVI threshold method (Sobrino et al., 2004). For the 2010 acquisition, we applied a gap-filling procedure to correct the Landsat 7 ETM+ Scan Line Corrector failure (SLC-off) using focal mean interpolation with an 11×11 kernel (Chen et al., 2011). We exported LST outputs at 30 m spatial resolution and clipped them to Senegal's national boundary. The retrieval procedure comprises six sequential steps described by Equations (1) through (5).

In the first step, we convert raw digital number (DN) values from the thermal band to at-sensor spectral radiance (top-of-atmosphere, TOA) using equation 1.

$$L_\lambda = M_L \times Q_{cal} + A_L \qquad (1)$$

where L_λ is the TOA spectral radiance ($W \cdot m^{-2} \cdot sr^{-1} \cdot \mu m^{-1}$), M_L is the band-specific multiplicative rescaling factor (RADIANCE_MULT_BAND), Q_{cal} is the quantized pixel value (DN), and A_L is the band-specific additive rescaling factor (RADIANCE_ADD_BAND).

The TOA spectral radiance is then converted to at-sensor brightness temperature (T_B) in Kelvin using equation 2:

$$T_B = \frac{K_2}{ln\left(\frac{K_1}{L_\lambda}+1\right)} \qquad (2)$$

where T_B is the brightness temperature in Kelvin, and K_1 and K_2 are sensor-specific thermal calibration constants provided in the Landsat metadata (Table 3).

Table 3. Thermal calibration constants for Landsat sensors used in this study

Sensor	K_1 (W/(m²·sr·µm))	K_2 (K)
Landsat 5 TM	607,76	1260,56
Landsat 7 ETM+	666,09	1282,71
Landsat 8 TIRS	774,89	1321,08

To estimate land surface emissivity, the percentage of vegetation cover (Pv) is first derived from NDVI using equation 3:

$$P_v = \left(\frac{NDVI - NDVI_{min}}{NDVI_{max} - NDVI_{min}}\right)^2 \qquad (3)$$

where P_v is the fractional vegetation cover, NDVI is the pixel-level normalized difference vegetation index, $NDVI_{min}$ and $NDVI_{max}$ are the threshold values for bare soil and fully vegetated surfaces, respectively.

The surface emissivity (ε) is then estimated using the approach of Sobrino et al. (2004) and is expressed by equation 4:

$$\varepsilon = 0{,}004 \times P_v + 0{,}986 \qquad (4)$$

This formulation assigns an emissivity of 0.986 to bare soil surfaces and up to 0.990 to fully vegetated surfaces.

Finally, the LST is computed by applying the emissivity correction to the brightness temperature using equation 5:

$$LST = \frac{T_B}{1 + \left(\frac{\lambda \times T_B}{\rho}\right) \times ln(\varepsilon)} \qquad (5)$$

where λ is the effective wavelength of the thermal band (λ = 10.8 µm for Landsat 8 Band 10, λ = 11.45 µm for Landsat 5/7 Band 6), and ρ = h × c / σ = 1.438 × 10^{-2} m·K (where h is Planck's constant, c is the light speed, and σ is the Boltzmann constant), and ε is the land surface emissivity.

2.5 Supervised Heat Stress Classification (2024)

Heat stress was mapped across the eight study cities using a Random Forest classifier (Breiman, 2001) implemented in Google Earth Engine. Three input features were selected: LST (2024, retrieved following the procedure in Section 2.4), NDVI, and the Normalized Difference Built-up Index (NDBI; Zha et al., 2003), all derived from Landsat 8/9 OLI-TIRS imagery acquired during the dry-season peak (March–June 2024, cloud cover <10%). We defined heat-stress thresholds based on established physiological benchmarks from the literature (Ndiaye et al., 2020; Santamouris, 2015).

Table 4. Heat-stress classification thresholds and physiological interpretation (Kotharkar & Ramesh, 2023; WHO, 2021).

Stress Level	LST Range (°C)	Physiological Interpretation	Recommended Response
Low	< 28	Thermal comfort; minimal physiological strain	Normal activities
Moderate	28-32	Moderate heat strain; risk for vulnerable groups	Vigilance; avoid sustained exertion
High	32-36	Strong heat strain; risk for most individuals	Hydration; shade mandatory
Extreme	> 36	Danger; severe heat stroke risk	Urgent protective measures

Training samples were generated using stratified random sampling, yielding 500 reference points per stress class. Samples were split 70/30 for classifier training and independent validation. The Random Forest classifier was configured with 100 decision trees. Assessment on the independent validation set yielded a mean overall accuracy of 98.1% and a Kappa coefficient exceeding 0.93 across all eight cities, confirming the reliability and consistency of the classification. The resulting heat stress maps were exported as GeoTIFF files for each city.

2.6 LCZ–Heat Stress Cross-Analysis

For each city, the LCZ vector layer and the 2024 heat stress raster were co-registered to a common coordinate reference system (UTM Zone 28N, WGS84, EPSG:32628). The area (m²) of each heat stress class within each LCZ polygon was extracted using the *exact_extract* function from the R *exactextractr* package (Baston, 2023). For each LCZ–city combination, the proportional area distribution across stress classes and the mean stress score ($\bar{S}$, ranging from 0 = low stress to 3 = extreme stress) were computed using equation 6:

$$\overline{S} = \frac{\sum(S_i \times A_i)}{\sum A_i} \quad (6)$$

where $S_{i\in\{0,1,2,3\}}$ is the stress level assigned to class *i,* and A_i is the corresponding area within the LCZ polygon. Differences in $\bar{S}$ across LCZ classes were tested for statistical significance using the Kruskal–Wallis nonparametric test ($\alpha = 0.05$), followed by Dunn's post-hoc test with Bonferroni correction for pairwise comparisons. We computed Spearman rank correlations between $\bar{S}$ and key morphological indicators, including building surface fraction (BSF), previous surface fraction (PERVF), and sky view factor (SVF), to identify the primary morphological drivers of thermal exposure. We also overlaid LCZ and heat stress maps to visually assess the spatial coherence of thermal hotspots across the eight cities.

3. Results

3.1 Land cover dynamics and urban expansion (2000–2020)

The land cover maps (**Fig. 3**) show a rapid, sustained transformation of the Senegalese landscape over the study period. Agricultural surfaces declined sharply from 2000 to 2020 (**Fig. 3a-c**), while built-up (red) surfaces expanded progressively, particularly in the metropolitan regions of Dakar, Touba, and Thiès (**Fig. 3d**). Built-up surfaces grew from 6700 km² in 2000 to 11070 km² in 2010 (+65%), then to 18090 km² in 2020 (+63%), representing a cumulative gain of 11390 km² (+170%) over two decades, as shown in Table 5. The rate of expansion accelerated markedly between decades: +4370 km² during 2000–2010 versus +7020 km² during 2010–2020. These trajectories align with the broader West African urbanization trend documented by Güneralp et al. (2017), who projected a tripling of built-up surfaces across Sub-Saharan Africa by 2050.

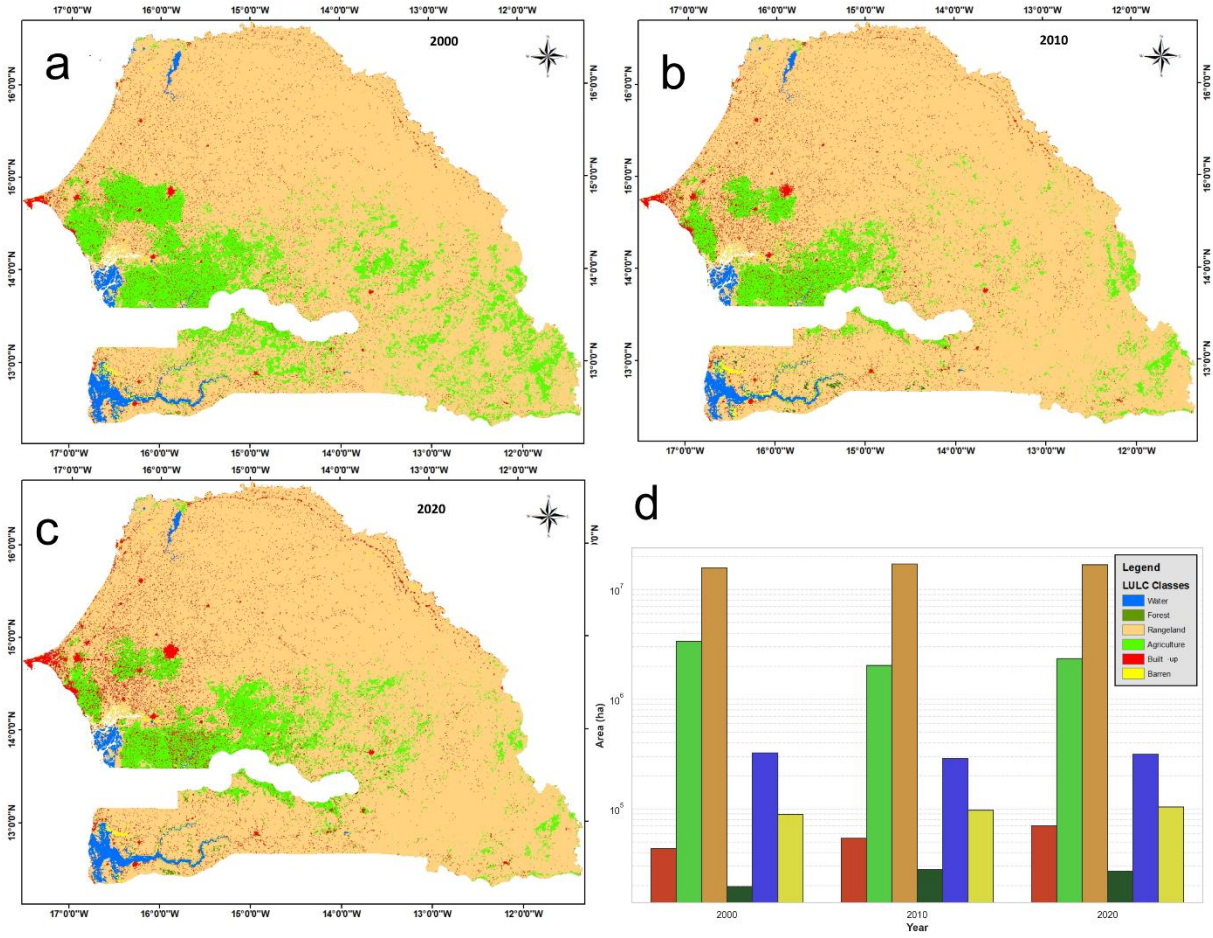


Fig. 3. Land use/land cover (LULC) maps of Senegal for 2000, 2010, and 2020, and evolution of area by class over the study period.

Table 5. Evolution of built-up surfaces in Senegal, 2000–2020.

Period	Built-up area (km²)	Absolute change (km²)	Relative change (%)	Annual rate (km²/yr)
2000	6700	--	--	--
2010	11070	+4370	+652	+437
2020	18090	+7020	+634	+702
2000-2020	--	+11390	+1700	+570

Fig. 4 shows the land-cover transition to built-up land from 2000 to 2020. Savanna and agricultural land are the two dominant sources of new built-up areas, accounting for 61.1% (218300 ha) and 37.3% (133100 ha) of the total converted area, respectively (**Fig. 4a**). Savanna conversion accelerated substantially between the two decades, rising from 506 km² during 2000–2010 to 1497 km² during 2010–2020 (+76% increase), while agricultural conversion grew by +31% over the same interval (**Fig. 4b-c**). At the city scale, Dakar (+157 km²), Touba (+92 km²), and Thiès (+68 km²) recorded the largest absolute expansions over the full 2000–2020 period.

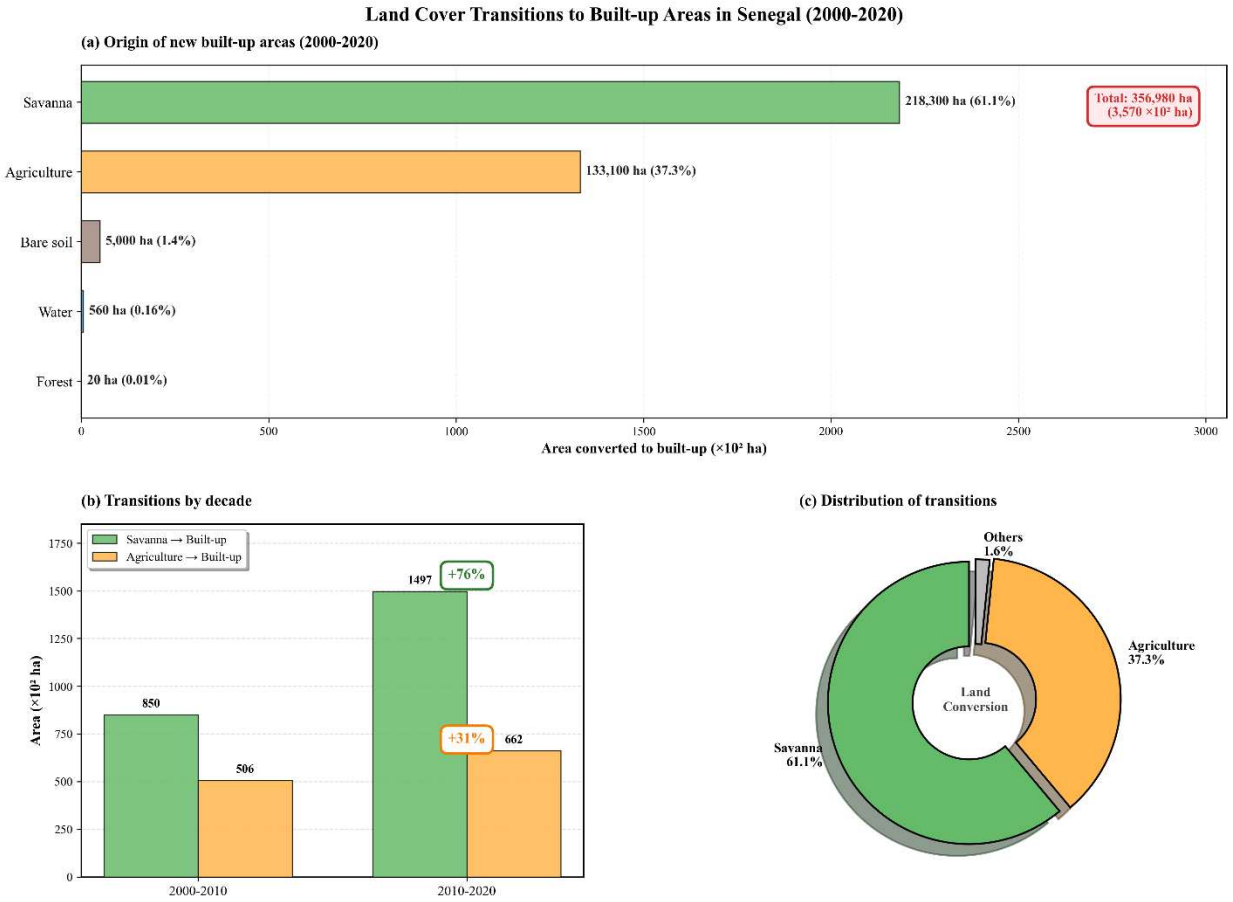


Fig. 4. Land cover transitions to built-up areas in Senegal (2000–2020). (a) Origin of new built-up surfaces (2000–2020): savanna (61.1%) and agricultural land (37.3%) are the dominant conversion sources. (b) Transitions by decade: marked acceleration in savanna conversion during 2010–2020 (+76%). (c) Proportional distribution of transitions.

3.2 Local Climate Zone Mapping

The LCZ maps for the eight Senegalese cities (**Fig. 5**) reveal striking morphological diversity, shaped by each city's historical heritage, climate, and urbanization trajectory.

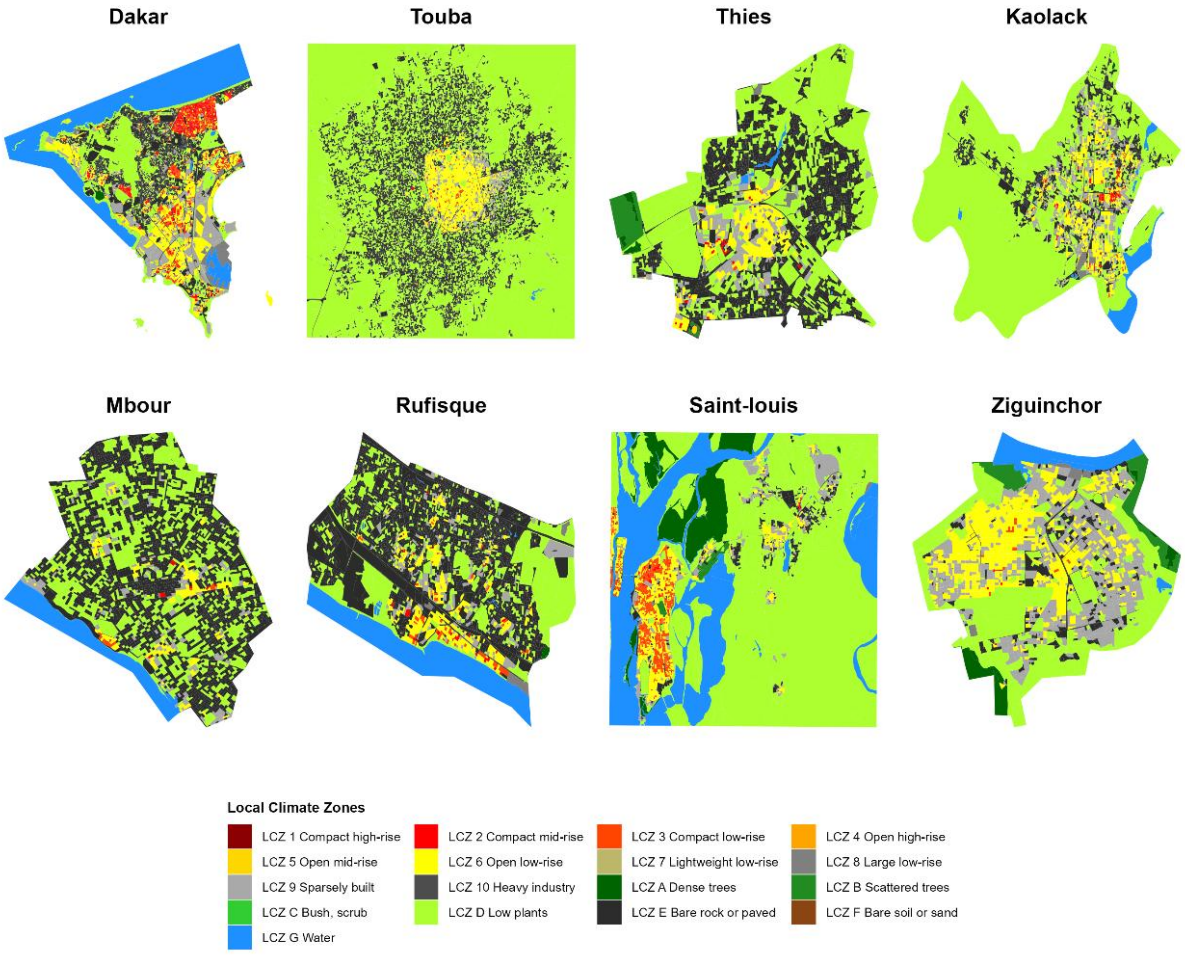


Fig. 5. Local Climate Zone (LCZ) maps of the eight Senegalese cities studied. Classification produced using GeoClimate v1.0 from OpenStreetMap data (2024). Classes 1–10 represent built-up types, and classes A–G represent natural land cover types.

Dakar exhibits the most complex LCZ mosaic in the study, confined to the Cape Verde Peninsula. The northeastern sector concentrates compact built-up classes (LCZ 1, 2, and 3) in a dense, interlocking pattern. The central sector is occupied by the extensive Forest Park (LCZ C and D), the only notable natural thermal sink on the map. The northwestern fringe alternates open low-rise

development (LCZ 6) with low vegetation (LCZ D), allowing sea-breeze penetration toward the interior. The eastern port-industrial corridor concentrates heavy industry (LCZ 8).

Touba displays the most homogeneous and morphologically singular profile: a near-uniform scatter of LCZ 7 (lightweight low-rise) organized in concentric aureoles around the Grand Mosque complex. The few LCZ 4–5 polygons corresponding to religious structures are concentrated in the central core, with a BSF of 58%, the highest recorded in the study, and a total absence of natural classes A, B, or G, depriving the city of any natural thermal regulation mechanism.

Thiès and Kaolack share a bipolar organization: a compact center (LCZ 3) surrounded by an open periphery (LCZ 6–7) inherited from the colonial urban plan. **Thiès** is distinguished by an LCZ A block (classified forest) in its northwestern quadrant, the only intra-urban natural thermal refuge, whereas **Kaolack** is characterized by the Saloum River (LCZ G) in its southeastern sector.

Mbour and Rufisque are both dominated by the open, low-rise fabric (LCZ 6) set against a low-vegetation background (LCZ D). **Mbour** exhibits a looser, more fragmented pattern characteristic of incremental, subdivision-based urbanization, whereas **Rufisque** has a higher building density in its historic center and a clearly delineated industrial zone (LCZ 10) along the national highway.

Saint-Louis is the most immediately legible map: the dominant water surface (LCZ G, the Senegal River, and the Langue de Barbarie lagoon) frames the historic island in the western sector, which is entirely classified as LCZ 3, reflecting its compact colonial morphology of narrow streets and courtyard buildings, and the continental district to the east, classified as LCZ 6–7.

Ziguinchor is the most morphologically diverse city in green-blue infrastructure: the central built-up fabric (LCZ 5–6) is embedded within peri-urban forests (LCZ A) and scattered tree zones (LCZ B), and it is bordered to the north by the Casamance River (LCZ G). Five of seven natural classes are present within the study perimeter, a unique configuration that directly explains the thermal resilience profile documented in the following sections.

3.3 Spatiotemporal variability of Land Surface Temperature (2000–2020)

3.3.1 National spatial structure and differentiated thermal regimes

The national mean LST, computed across all terrestrial pixels of Senegal, showed a statistically significant increase from 2000 to 2020 (Mann–Kendall $\tau = 0.89$, $p < 0.01$), rising from 35.2 °C in

2000 to 35.9 °C in 2010 and 36.4 °C in 2020, corresponding to a cumulative warming of +1.2 °C over two decades. This rate, approximately +0.06 °C per year, exceeds the global mean surface warming of +1.1 °C estimated over the entire twentieth century (IPCC AR6; Masson-Delmotte et al., 2021), reflecting the superposition of the global climate signal and a local anthropogenic signal driven by urban expansion and vegetation loss. It is consistent with LST trends of +0.5 to +1.5 °C reported over comparable periods in other studies of West African cities (Diallo et al., 2020; Ermert et al., 2023).

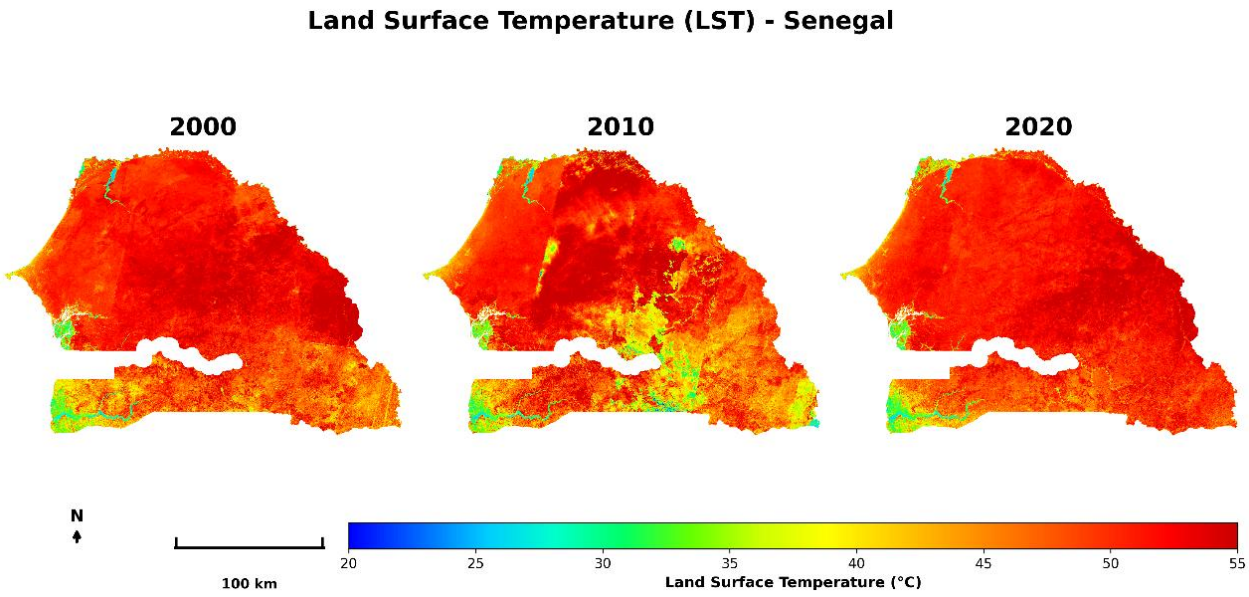


Fig. 6. Spatiotemporal dynamics of Land Surface Temperature (LST) across Senegal (2000–2020). Images derived from the Landsat archive (Collection 2, Level-2) processed on Google Earth Engine. The color scale ranges from 20 °C (blue) to 55 °C (dark red).

Fig. 6 shows the three national LST maps and reveals a spatially stable yet increasingly intense pattern. A well-defined meridional gradient structures Senegalese territory at all three dates: the Sahelian north encompassing the regions of Louga, Matam, and northern Touba is dominated by LST values of 45–55 °C, whereas southern Casamance displays LST values of 25–33 °C, attributable to dense forest cover and high evapotranspiration sustained by annual rainfall exceeding 1,000 mm. This nearly 20 °C latitudinal contrast between north and south is the figure's dominant signal and faithfully reflects the country's bioclimatic zonation (Tall et al., 2020). In 2000, LST distribution showed a relatively homogeneous texture across the northern two-thirds of

the territory. Three features stood out: the Senegal River recording LST values below 25 °C, confirming watercourses as thermal sinks in arid environments; the Cape Verde Peninsula displaying LST values of 28–33 °C, attributable to the moderating effect of the Canary Current's coastal upwelling; and the Casamance forest cover recording LST values of 25–30 °C, markedly cooler than its surroundings. The 2010 map is the most spatially heterogeneous of the three, characterized by an extensive zone recording LST values of 28–36 °C across the center-west and the groundnut basin. Two non-mutually exclusive mechanisms explain this relative cold anomaly: first, the 2000–2010 decade coincides with a documented Sahelian rainfall recovery widely referred to as the "Sahel re-greening" (Mbow et al., 2020), which increases residual vegetation cover and latent heat fluxes from savanna surfaces; second, the Landsat 7 acquisition date for 2010 may have captured a slightly earlier phenological window than those for 2000 and 2020. The heterogeneous texture of the center-west in 2010, with corridors of LST below 33 °C along hydrological axes and seasonal streams, supports the first interpretation. This observation matters because it suggests the warming trend between 2000 and 2020 is likely underestimated if 2010 is used as an intermediate reference year. By 2020, the LST pattern is both more extensive and more intense than in 2000. The central cooling observed in 2010 has almost entirely disappeared, indicating that the surface energy balance has shifted under the combined effects of built-up expansion (+63% relative to 2010), accelerated savanna loss, and reduced soil water availability. The Casamance retains LST values of 25–33 °C but over a smaller area, while LST values of 33–38 °C infiltrate peri-urban deforestation zones north of Ziguinchor. Along the Atlantic coast, the band of LST values below 32 °C in 2020 is markedly narrower than in 2000, reflecting the progressive erosion of the maritime moderation buffer by coastal urbanization in Dakar, Mbour, and Rufisque. Taken together, three thermal regimes persistently structure Senegalese territory: (i) a hyper-hot Sahelian regime (> 45 °C) in the north and east, temporally stable and macroclimatically determined; (ii) an intermediate Sudano-Sahelian regime (38–45 °C) in the center, strongly modulated by interdecadal rainfall fluctuations and built-up expansion; and (iii) a cool Sudano-Guinean regime (< 35 °C) in the south, whose thermal resilience is directly contingent on the maintenance of forest cover.

3.3.2 Comparative analysis of urban thermal profiles.

Circular zone representation has been used to analyze and compare the urban thermal profiles of selected Senegalese cities. **Fig. 7** enables both longitudinal and transverse readings, providing analytical power beyond mean values alone. It reveals each agglomeration's internal spatial structure, local thermal sinks, and how these configurations evolved over twenty years.

Dakar exhibits an atypical thermal profile that intensifies over time. The intra-urban thermal contrast is the strongest in the entire dataset: in 2000, the western coastal fringe and the northwestern tip of the peninsula display LST values of 25–32 °C, while the central-eastern districts reach 40–44 °C, an intra-urban thermal differential of 10–15 °C attributable to the Atlantic Sea breeze and the upwelling of the Canary Current (Tall et al., 2020). This coastal–inland gradient remains structurally intact in 2020 despite the densification of the coastal built-up front; the fraction of surfaces recording LST values below 32 °C declines visibly, reflecting the progressive erosion of the maritime moderation effect. Dakar is the only city in this study to show persistent low-LST pixels (< 25 °C) across all three dates, driven by the water bodies along the coastline and the eastern bay.

Touba represents the polar opposite case. By 2000, the entire circular zone was saturated with LST values ranging from 45 to 52 °C, with no visible thermal heterogeneity. The complete absence of surfaces recording LST values below 36 °C is not trivial; it indicates that no functional green space, water body, or pervious surface of significant size exists within the 5 km radius. This thermal homogeneity intensifies slightly between 2000 and 2020, as the granular texture of the light-colored bare soils visible in 2000 progressively gives way to a more uniform high-LST signature (> 45 °C) associated with the generalization of metal roofing and paved surfaces (car parks, roads). With urban core LST values reaching 49.0 °C in 2020 and no accessible thermal refuge, Touba is the most alarming example of a Sahelian city with LCZ 7 morphology and no cooling infrastructure.

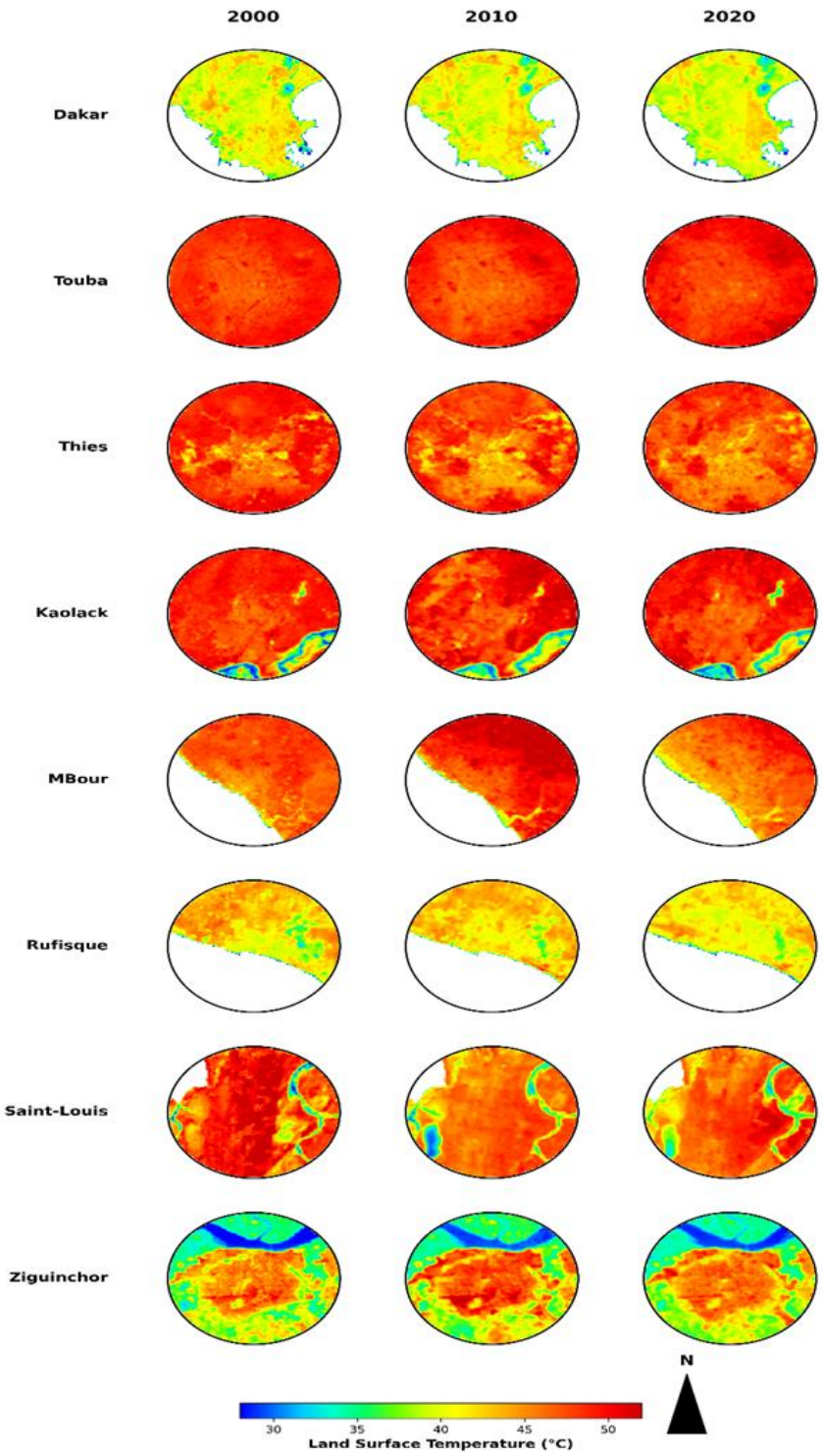


Fig. 7. Thermal evolution of the eight major urban centers of Senegal (2000–2020), analyzed through circular buffer zones (5 km radius). Each row corresponds to a city; each column to a reference year (2000, 2010, 2020). The color scale ranges from 30 °C (blue) to 50 °C (dark red).

Thiès illustrates the process of "residual greening displacement". In 2000, the central zone recorded LST values of 28–35 °C, corresponding to classified forest and colonial green spaces, in sharp contrast to the periphery, which recorded 40–48 °C. By 2010, this cooler central zone had contracted, and by 2020 it was nearly absent, indicating that unplanned expansion had progressively absorbed the central green spaces and homogenized the urban thermal signature toward higher values. This trajectory exemplifies progressive thermal lock-in in rapidly growing cities (Seto et al., 2016).

Kaolack is notable for the persistence, across all three dates, of a cool sector in the southeastern quadrant of its circular zone recording LST values of 25–30 °C. This cool signal corresponds to the Saloum River and its lagoonal branches, whose LST of 25–30 °C contrasts sharply with the surrounding city's 44–48 °C, a 15–20 °C differential that quantifies the oasis effect of urban fluvial corridors. The cooling extends 400–600 m from the riverbank, consistent with values reported by Mushore et al. (2017) for comparable watercourses in southern Africa. However, the progressive reduction of this cool sector between 2000 and 2020, with surfaces recording LST values above 40 °C advancing toward the riverbank, reflects the densification of built-up land along the riparian zone, which gradually reduces the depth and spatial extent of the fluvial thermal halo.

Mbour and Rufisque, both coastal cities, have about half of their circular zones covered by the ocean, limiting the analysis to terrestrial surfaces. In Mbour, land surface temperatures rose from approximately 35–38 °C in 2000 to 40–44 °C in 2020, reflecting a net warming of 2–3 °C associated with residential and tourist densification. Rufisque benefits from slightly greater maritime moderation because of its proximity to the Cape Verde Peninsula, with land surfaces remaining predominantly in the 38–43 °C range in 2020, about 2–3 °C cooler than Mbour's inland sectors over the same period. A band of low-LST pixels (< 30 °C) appears along the northeastern bay shoreline in 2020 but is absent in 2000, most likely due to the extension of tidal mudflats and degraded mangroves, whose thermal spectral signature is substantially lower than that of built-up surfaces.

Saint-Louis presents the most complex map to interpret because two thermally dominant water bodies abut it: the Senegal River to the east and the Langue de Barbarie lagoon to the west. In 2010, the cool surface associated with the river, with LST values below 28 °C, expanded

noticeably, consistent with the documented flood extension following exceptionally high rainfall in the upper Senegal River basin during that decade. This pattern shows that Saint-Louis's LST dynamics are driven as much by the river's hydrological regime as by urban morphology, a unique feature among the eight cities studied that warrants particular caution when interpreting its LST values in cross-city comparisons.

Ziguinchor exhibits the most remarkable thermal resilience profile. As early as 2000, the circular zone displays unparalleled LST diversity: an intense cool band to the north corresponding to the Casamance River (LST < 25 °C); a mosaic of surfaces with LST values of 25–35 °C covering 50–60% of the total area, associated with dense forest cover and irrigated market gardens; and a high-LST zone (> 40 °C) confined to the built-up city center. By 2020, this fundamental structure is maintained: the river retains its low LST signature (< 25 °C), peri-urban forest zones record LST values of 25–33 °C, and the fraction of surfaces with LST values above 40 °C remains below 30% of the circular zone, the lowest value recorded in the study. This 20-year thermal stability empirically demonstrates that maintaining sufficiently dense urban forest cover (canopy fraction > 60%, LCZ A class), combined with a perennial watercourse, is the most effective thermal regulation mechanism in the humid West African urban context.

3.4 Heat Stress Mapping (2024)

Fig. 8 presents the 2024 heat stress maps for the eight cities studied, generated by the Random Forest classifier, which achieved 98.1% overall accuracy and a Kappa coefficient of 0.936. Severe, widespread thermal exposure is observed across all eight Senegalese cities, highlighting a spatially structured vulnerability hierarchy governed by the coastal–inland macroclimatic dichotomy and the presence or absence of natural thermal-regulation infrastructure.

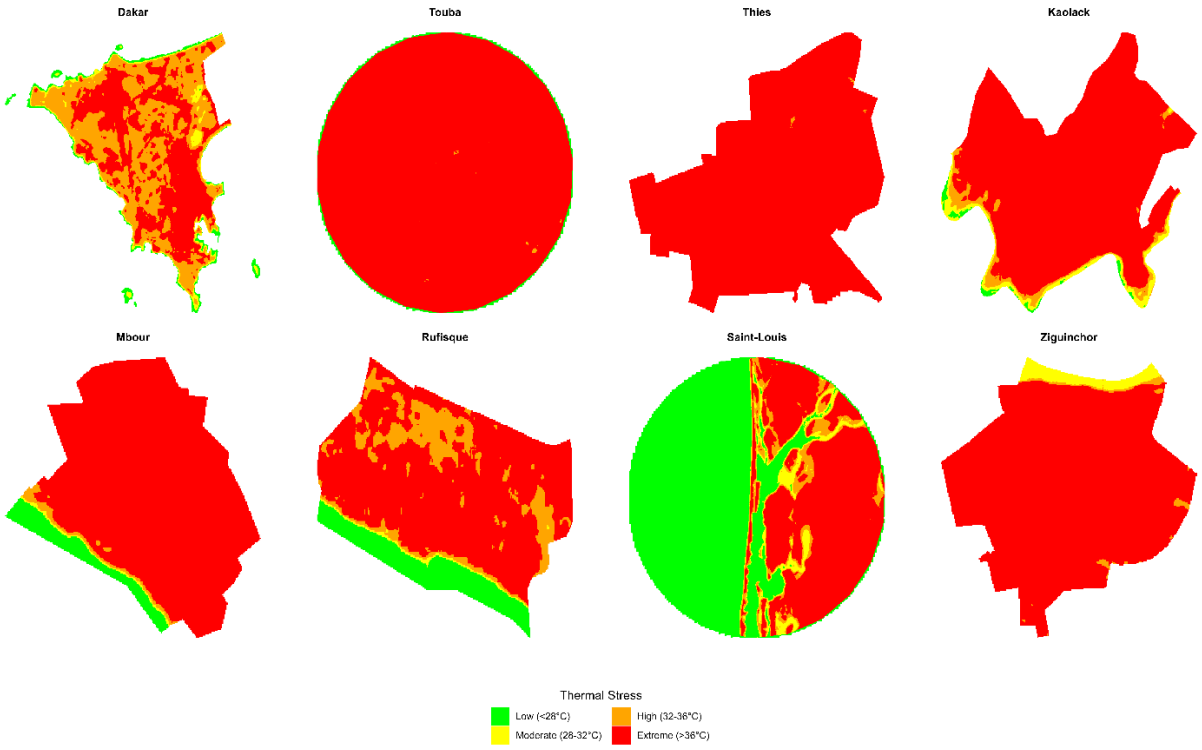


Fig. 8. Heat stress maps (2024) for the eight Senegalese cities studied.

At one end of the spectrum, **Touba** shows complete saturation under extreme heat stress (LST > 36 °C) across its entire urban perimeter, with no identifiable thermal refuge pixels within the built-up boundary. This pattern is driven by a dominant LCZ 7 morphology (metal roofing, bare soil, and a lack of functional vegetation) and a Sahelian macroclimate with no external moderation, posing a first-order public health risk for its 1.19 million inhabitants. **Thiès** shows a similar configuration, with residual moderate-to-high stress patches (LST 32–36 °C) confined to colonial-era green spaces and covering less than 10% of the urban area. **Kaolack**, despite comparable extreme stress saturation (LST > 36 °C) across most of its built fabric, benefits from a remarkable cooling corridor along the Saloum River (LST < 28 °C). This oasis effect, extending 300–500 m from the riverbank, illustrates both the potential and the limitations of fluvial thermal sinks amid uncontrolled riparian urbanization.

At the opposite end, the coastal cities of **Mbour**, **Rufisque**, and **Dakar** display a characteristic ocean-to-inland thermal gradient: a band of low-to-moderate stress (LST < 32 °C, 300–800 m in depth) along the Atlantic fringe, driven by the sea breeze, which dissipates rapidly once the

continuous built-up fabric blocks ventilation. Central and peri-central districts are often the most densely populated and economically deprived, experiencing high-to-extreme stress (LST > 36 °C). **Dakar** stands out for the greatest stress-class diversity among the eight cities, with persistent low-stress zones (LST < 28 °C) along the peninsula's northwestern tip and around the central Forest Park, indicating that large-scale green spaces are the only effective thermal refuges within a compact urban fabric.

Saint-Louis exhibits the most spatially polarized configuration. The Senegal River occupies about 45% of the study area and records low-stress temperatures (LST < 28 °C), whereas the eastern continental district is uniformly classified as extreme stress (LST > 36 °C). This represents one of the most pronounced intra-urban thermal inequalities in the dataset, with two locations less than 500 m apart differing by more than 20 °C in LST solely because of the presence or absence of the water body.

Ziguinchor exhibits the most nuanced resilience profile. While most of the built-up area records extreme stress (LST > 36 °C) under the dry-season Sudano-Guinean macroclimate, the Casamance River produces the deepest cooling halo in the study (LST < 28 °C, extending 300–500 m from the bank). The historically tree-lined districts of the central-western sector maintain moderate-to-high stress temperatures (LST 32–36 °C) due to shading and evapotranspiration from large-canopy trees, in striking contrast to the recently densified northeastern sector, where urbanization removed vegetation cover and surfaces uniformly record extreme stress (LST > 36 °C). This demonstrates that, as in all cities studied, the conservation or destruction of vegetation cover during urbanization ultimately determines, at the city-block scale, the population's level of thermal exposure.

3.5 LCZ–Heat Stress Cross-Analysis

The LCZ–heat stress cross-analysis is shown in Figures 9 and 10. It is based on the mean stress score $\bar{S}$ computed across all city–LCZ class combinations and tested for statistical significance using the Kruskal–Wallis test ($H = 143.7$, $df = 13$, $p < 0.001$). Taken together, the two figures yield three major findings that capture the comparative structure and contextual nuances.

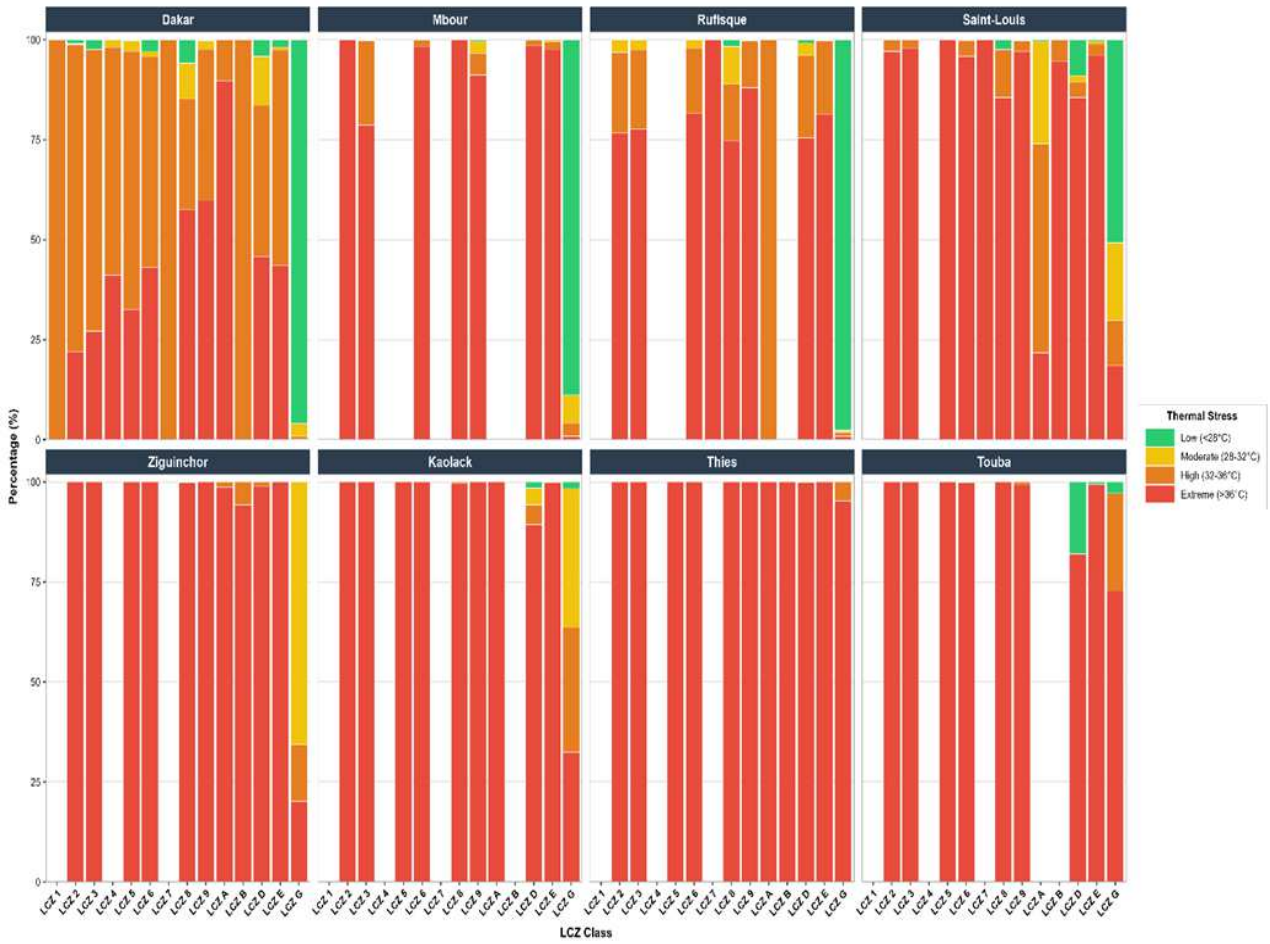


Fig. 9. Distribution of heat stress levels by LCZ class for the eight Senegalese cities (2024). Each stacked bar indicates the proportion (%) of surfaces classified as low stress (< 28 °C), moderate stress (28–32 °C), high stress (32–36 °C), and extreme stress (> 36 °C) within each LCZ class.

First, the analysis confirms a robust, hierarchically ordered inter-class thermal gradient. The heatmap (Figure 10) shows that compact built-up classes LCZ 2 and LCZ 3, as well as impervious non-built surfaces LCZ E (bare rock or paved), display the highest $\bar{S}$ scores across the dataset, systematically approaching 3 (extreme stress) in all cities where they occur. By contrast, LCZ G (water) is the only class whose score consistently remains low, between 0 and 1, irrespective of city. This finding is corroborated by the stacked bar charts in **Fig. 9**, where the LCZ G column is the only one showing a majority of green in the cities where it is present (Saint-Louis, Kaolack, Ziguinchor, and Rufisque).

Second, the heatmap shows macroclimatic effects as a systematic modifier of stress level at constant morphology. Dakar, with $\bar{S}$ values consistently ranging from 1.5 to 2.0 across all LCZ classes, is structurally distinct from all other cities, where $\bar{S}$ values systematically exceed 2.5. This reflects a global downward shift in $\bar{S}$ of 0.5–0.8 points relative to inland cities within each comparable LCZ class. This implies that an LCZ 6 zone (open low-rise) in Dakar ($\bar{S} \approx 1.8$) is thermally equivalent to an LCZ 9 zone (sparsely built) in Touba or Thiès ($\bar{S} \approx 1.9$–2.0). Conversely, Touba, Thiès, and Ziguinchor show nearly saturated heat stress ($\bar{S}$ values approaching 3.0) across nearly all LCZ classes. These patterns confirm that the Sahelian macroclimate or compact morphology suppresses observable inter-class differences, except in LCZ G, which records $\bar{S}$ values below 1.0 in Ziguinchor and is absent in Touba.

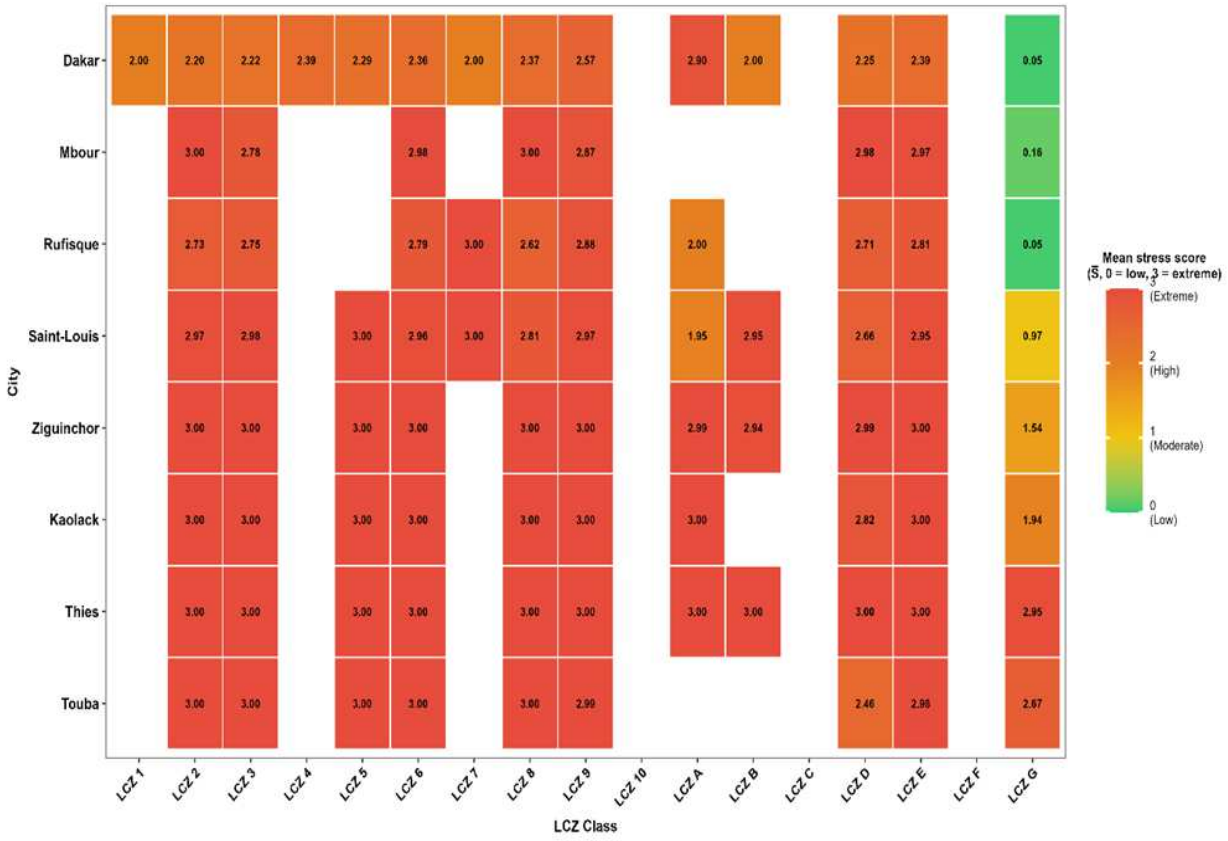


Fig. 10. Heatmap of mean heat stress scores ($\bar{S}$) by LCZ class and city. The color scale ranges from 0 (low stress, green) to 3 (extreme stress, dark red). White cells indicate that the LCZ class is absent within the city perimeter.

Third, the LCZ A paradox of dense trees is the most scientifically original finding in Fig. 10. It is the only natural class whose $\bar{S}$ score varies drastically across cities, ranging from 1.1 in Ziguinchor to 2.7 in Touba. Ziguinchor's low $\bar{S}$ score reflects dense canopy cover, a functional riparian forest, and high soil moisture that sustain evapotranspiration, whereas in Touba, LCZ A zones correspond to open palm groves with canopy cover below 40% and cannot offset the Sahelian radiation budget. In the stacked bar charts in Fig. 9, LCZ A in Touba shows more than 95% of surfaces in the extreme-stress category (LST > 36 °C), whereas Ziguinchor shows a substantial proportion of surfaces in the moderate-to-high-stress category (LST: 28–36 °C). This immediate, quantifiable contrast empirically demonstrates that LCZ A classification alone cannot reliably proxy tree cooling services in arid contexts and must be systematically complemented by canopy-density indicators, specifically the Enhanced Vegetation Index (EVI) and Leaf Area Index (LAI). These two indicators can accurately assess urban cooling potential in Sahelian cities. Finally, Spearman rank correlations confirm that building surface fraction (BSF, $\rho = 0.74$, $p < 0.001$) and pervious surface fraction (PERVF, $\rho = -0.71$, $p < 0.001$) are the two primary morphological determinants of $\bar{S}$, identifying these parameters as the priority levers for thermal regulation through urban design policy in Senegalese cities.

4. Discussions

4.1 Urbanization as the primary driver of surface warming: Thermal lock-in and irreversibility

Our findings show that the accelerated expansion of built-up surfaces (+170% over 2000–2020), with 61.1% of conversions drawn from savanna and 37.3% from agricultural land, is the dominant proximal driver of surface warming in Senegal. This pattern aligns with global meta-analyses by Peng et al. (2012) and Zhou et al. (2017), as well as the West African urbanization trajectories modeled by Güneralp et al. (2017). Beyond conversion volume, the nature of the converted land determines the magnitude of warming. The savanna-to-built-up transition is more thermally penalizing than the agriculture-to-built-up transition because savanna maintains latent heat fluxes of 80–150 $W \cdot m^{-2}$ and an albedo of 0.15–0.20, substantially higher than that of metal roofing (0.10–0.12). Its replacement simultaneously reduces the latent heat partition and increases anthropogenic heat storage, consistent with the urban energy balance framework formalized by Oke et al. (2017).

The acceleration of savanna conversion over 2010–2020 (+76%) coincides with the Senegalese government's "Plan Senegal Emergent (PSE)" program (PSE; Government of Senegal, 2014). The PSE infrastructure programs catalyzed intensive peri-urbanization on unprotected lands, exemplifying Seto et al.'s (2016) thermal lock-in concept. Current land-use decisions commit Senegalese cities to potentially irreversible thermal trajectories over generational timescales, as reconverting sealed surfaces into functional green spaces is far more costly, economically and socially, than protecting them initially. With projections of built-up surfaces doubling across Sub-Saharan Africa by 2050 (Güneralp et al., 2017), integrating peri-urban savanna conservation thresholds into Senegalese Urban Master Plans (Plans Directeurs d'Urbanisme, PDU) is an adaptation priority for which our data provide direct quantitative justification.

4.2 LCZ Morphology as a physical determinant of thermal exposure

The LCZ–heat stress relationship (Kruskal–Wallis $H = 143.7$, $p < 0.001$), corroborated by significant Spearman rank correlations between $\bar{S}$ and building surface fraction (BSF, $\rho = 0.74$) and pervious surface fraction (PERVF, $\rho = -0.71$), empirically validates the LCZ framework's founding postulate for Senegalese cities. It confirms that urban morphology is a first-order determinant of the surface microclimate (Stewart & Oke, 2012). This result aligns with global validations by Demuzere et al. (2022) and african evidence from Bechtel et al. (2019). Three synergistic physical mechanisms explain the BSF–LST relationship shown in the heatmap (**Fig. 10**). A reduced sky view factor (SVF) traps shortwave radiation within urban canyons and suppresses nocturnal radiative cooling (Oke et al., 2017). Surface sealing eliminates evapotranspiration by concentrating net energy into sensible heat flux and material thermal storage (Grimmond, 2007). The dominant construction materials in Senegalese cities (concrete, corrugated metal, and laterite) have high thermal admittance, maximizing diurnal heat storage and nocturnal heat release (Balogun et al., 2020). Touba's LCZ 7 class, with a BSF of 58% and metal roofing reaching 65–75 °C under direct solar exposure, combines all three mechanisms at maximum intensity. Conversely, LCZ G (water) shows the lowest $\bar{S}$ scores in the dataset (0.3–0.8), regardless of city, and confirms the irreplaceable role of water bodies as primary thermal sinks with a cooling reach of 200–500 m, consistent with Mushore et al. (2017). Identifying BSF and PERVF as priority morphological levers enables the formulation of normative thresholds that are directly operational

within urban planning regulations (BSF ≤ 40% and PERVF ≥ 25%) for new residential zones, without requiring complex climate modeling.

4.3 The LCZ A paradox: the limits of the "Green Equals Cool" paradigm in arid contexts

The study's most original finding is the strongly context-dependent thermal performance of LCZ A (dense trees), whose $\bar{S}$ score ranges from 1.1 in Ziguinchor to 2.7 in Touba, the largest inter-city variation among any class, built-up or natural. This challenges the universal applicability of the paradigm that tree vegetation reliably cools urban areas, a paradigm underpinning most urban greening policies in Africa (Venter et al., 2020). The combined reading of the LCZ maps (**Fig. 5**) and the heatmap (Figure 10) provides the mechanistic explanation. In Ziguinchor, LCZ A zones correspond to riparian forests with canopy cover exceeding 70%, benefiting from soil moisture maintained by 1200 mm of annual rainfall and generating sustained evapotranspiration of 3–5 $mm \cdot day^{-1}$ that reduces LST by 4–8 °C relative to adjacent built-up surfaces. In Touba, the same zones classified as LCZ A correspond to open palm groves and acacia woodlands with canopy cover below 40%, where evapotranspiration is near zero in the absence of soil moisture. As a result, partial shading fails to compensate for the infrared radiation emitted by the heated ground surface (Tan et al., 2020; Oliveira et al., 2011), and this aligns with observations reported by Manyanya et al. (2024) for Cape Town and Kotharkar and Ramesh (2023) for semi-arid Indian cities.

4.4 The Coastal–Sahelian dichotomy: macroclimatic modulation, fragility of the coastal advantage, and thermal inequalities.

The systematic $\bar{S}$ offset of 0.5–0.8 points between coastal and inland cities is visible across all LCZ classes in the heatmap (**Fig. 10**). Dakar records mean $\bar{S}$ values of 1.5–2.0 across all LCZ, in stark contrast to Sahelian cities, where $\bar{S}$ systematically exceeds 2.5. This indicates that the macroclimatic factor is a second-order modifier, with an amplitude comparable to a two-class LCZ shift: an LCZ 6 zone in Dakar ($\bar{S} \approx 1.8$) is thermally equivalent to an LCZ 9 zone in Touba ($\bar{S} \approx$ 1.9–2.0). This finding implies that thermal comfort standards and greening targets must be differentiated by climatic zone rather than applied uniformly at the national scale, in line with WHO (2021) recommendations on Heat-Health Action Plans. However, this coastal advantage is

itself under threat. Tropical North Atlantic warming and the projected reduction in Canary Current upwelling intensity under RCP 4.5 and 8.5 (Sylla et al., 2018; Camara et al., 2021) are expected to progressively erode the maritime moderation of Dakar, Mbour, and Rufisque, which currently maintain coastal LST values of 28–35 °C compared to 40–49 °C in inland cities. This dynamic is already underway: our LST maps show a measurable narrowing of the coastal band of LST values below 32 °C between 2000 and 2020 (**Fig. 6**). This makes it more urgent to build thermally resilient infrastructure in these cities, which cannot defer greening investments by invoking current maritime moderation as sufficient protection. Furthermore, our heat stress maps (Figure 8) reveal a structural intra-urban thermal inequality in coastal cities. Low-to-moderate stress zones (LST < 32 °C) are localized along the coastal fringe and accessible to the most affluent districts. Low-income populations in densified central neighborhoods face high-to-extreme stress (LST > 36 °C) without access to coastal thermal refuges, reproducing the geography of thermal vulnerability documented in Europe by Laaidi et al. (2012) and in North America by Heaviside et al. (2017). This situation underscores the need to make thermal justice a core dimension of any urban adaptation policy.

4.5 Implications for climate-resilient urban planning and adaptation policy.

In coastal cities, the top priority is protecting existing green-blue infrastructure. The Hann Forest Park in Dakar exemplifies this approach, with permanent no-build easements integrated into Urban Master Plans (PDU) and ventilation corridors perpendicular to the coastline to maintain sea-breeze penetration toward inland districts (Oke et al., 2017). In Sahelian cities, the strategy must combine tree species that provide sustained shade through the dry season (*Faidherbia albida*, Baobab, Neem). In addition, high-albedo roofing and surface treatments with albedo values from 0.10 to 0.60 can reduce LST by 1–3 °C in LCZ 7 environments (Santamouris et al., 2020). Regulatory protection of fluvial corridors, such as the Saloum River in Kaolack, is needed, as riparian densification is directly eroding the fluvial thermal halo visible on the heat stress map (Fig. 8). For Touba specifically, the extreme stress saturation affecting 1.19 million inhabitants justifies an emergency response that extends beyond conventional planning instruments. Equipping existing community structures (*daara*, mosques) as climate refuges with solar-powered misting systems offers an immediate, low-cost, and socially appropriate solution, analogous to the cooling centers deployed across Europe during heat waves (Laaidi et al., 2012). At the national scale, the LCZ and

heat stress maps produced in this study provide a direct, operational monitoring tool for tracking SDGs 11.1 and 13.1 and for spatially operationalizing Senegal's Nationally Determined Contribution (Government of Senegal, 2021). Annual updates of the LST composite from Landsat/Sentinel-2 and quinquennial LCZ revisions via GeoClimate are technically feasible at near-zero cost, given the open-access nature of all data and tools employed, and are institutionally scalable within the SERVIR West Africa network (SERVIR-WA, 2023).

5. Conclusion

This study presents the first integrated, multi-city characterization of urban morphology and thermal exposure in Senegal over 24 years (2000–2024), combining LCZ classification by GeoClimate, multi-temporal LULC analysis from MODIS/GHSL, Landsat LST retrieval on Google Earth Engine, and Random Forest heat-stress mapping. Its original contributions are fourfold: (i) the national multi-city LCZ dataset for Senegal; (ii) a spatially explicit assessment of 20 years of urban expansion and its thermal consequences; (iii) a heat-stress map validated at 98.1% overall accuracy; and (iv) the identification of an LCZ A paradox, i.e., the thermal ineffectiveness of tree-based greening in arid contexts, which constitutes an original contribution to the LCZ framework applicable to Sahelian cities across the region. Five principal findings frame these contributions.

Built-up surfaces expanded by 170% from 2000 to 2020, with 61.1% converted from savanna and 37.3% from agricultural land. The expansion accelerated by 30% during 2010–2020, attributable to infrastructure under the “Plan Sénégal Émergent” program, producing a statistically significant national warming of +1.2°C, with peaks of +1.8°C in Sahelian cities and an urban LST of 49.0°C in Touba in 2020 among the highest values documented for any West African city. LCZ mapping reveals contrasting morphological signatures, from the diverse mosaic of the Dakar peninsula to the radial, concentric homogeneity of Touba. Ziguinchor, which presents five of seven natural LCZ types, serves as a reference model of morphological resilience. The LCZ–heat stress cross-analysis (Kruskal–Wallis $H = 143.7$, $p < 0.001$) establishes a robust inter-class gradient hierarchized by building surface fraction (BSF, $\rho = 0.74$) and pervious surface fraction (PERVF, $\rho = -0.71$), two parameters directly translatable into operational regulatory standards (BSF $\leq 40\%$, PERVF $\geq 25\%$) without requiring additional climate modeling. The LCZ A paradox: dense trees are effective in Ziguinchor ($\bar{S} = 1.1$) but near neutral in Touba ($\bar{S} = 2.7$), demonstrating that the

standard LCZ framework overestimates the tree cooling service in arid contexts where canopy cover is discontinuous and soil moisture is negligible. Finally, the systematic $\bar{S}$ offset of 0.5–0.8 points between coastal and inland cities, persistent across all LCZ classes, establishes that the macroclimatic context acts as a second-order modifier with an effect comparable to a two-class LCZ shift, highlighting the need to differentiate urban heat adaptation strategies by climatic context. However, projected weakening of the Canary Current upwelling under RCP 4.5 and 8.5 (Sylla et al., 2018; Camara et al., 2021) may threaten this coastal moderation, with the measurable narrowing of the coastal cool-pixel band between 2000 and 2020 providing a potential early signal.

These findings provide Senegal's first national multi-city LCZ baseline, fill a major geographical gap in the WUDAPT database (Ching et al., 2018), and serve as the reference dataset for future WRF–SUEWS modeling of 2050 UHI scenarios. On the policy front, the 30 m resolution heat stress maps provide decision-makers with the spatial diagnostic tool previously lacking to operationalize Senegal's NDC commitments (Government of Senegal, 2021) and to report on SDG 11.1 and 13.1 indicators at the city-block scale. Urban heat in Senegal is not a climatic inevitability: it is, fundamentally, the product of morphological and land-use decisions that planning can change. The gap between Ziguinchor, where the maintenance of forest and fluvial cover limits extreme stress to less than 70% of the urban perimeter, and Touba, where its absence drives it to 100%, constitutes, more than any prospective modeling exercise, the strongest argument for a resolutely climate-informed urban planning approach in Senegal and across West Africa's Sahelian cities.

The LCZ maps and morphological metrics produced in this study for building surface fraction, sky view factor, and pervious surface fraction provide directly usable input data for physical modeling of the urban energy balance using the SUEWS scheme (Jarvi et al., 2011; Ward et al., 2016) and for projecting urban heat islands to 2050 by coupling with the WRF-Urban model under the RCP 4.5 and 8.5 scenarios (Skamarock et al., 2019). These developments naturally follow from the present work.

Ethical statement

It is stated that all ethical practices have been followed in relation to the development, writing, and publication of the article.

Declaration of competing interest

The authors declare that they have no known competing financial interests or personal relationships that could have appeared to influence the work reported in this paper.

Acknowledgments

No specific funds were available to conduct this research. The first author is thankful to all the institutes (mentioned within the text) for the provisioning of relevant data to carry out this valuable study. The research is conducted in the absence of any commercial or financial relationships that could be construed as a potential conflict of interest. All the data used for several analyses are freely available and the resources are mentioned within the paper.

References

Akbari, H., Cartalis, C., Kolokotsa, D., Muscio, A., Pisello, A. L., Rossi, F., Santamouris, M., Synnefa, A., Wong, N. H., & Zinzi, M. (2016). Local climate change and urban heat island mitigation techniques: The state of the art. *Journal of Civil Engineering and Management*, *22*(1), 1–16. https://doi.org/10.3846/13923730.2015.1111934

Agence nationale de la statistique et de la démographie (ANSD) (2024). *Projections démographiques 2023–2073*. Ministère de l'Économie, du Plan et de la Coopération, République du Sénégal.

Agence nationale de la statistique et de la démographie (ANSD) (2026). *Annuaire de la population du Sénégal : Année 2025*. République du Sénégal.

Arnfield, A. J. (2003). Two decades of urban climate research: A review of turbulence, exchanges of energy and water, and the urban heat island. *International Journal of Climatology*, *23*(1), 1–26. https://doi.org/10.1002/joc.859

Balogun, A. A., Balogun, I. A., Adefisan, E. A., Abatan, A. A., & Bayo, I. (2020). Urban heat island characteristics and its effects on outdoor thermal comfort in a tropical West African city. *Meteorology and Atmospheric Physics*, *132*(2), 185–198. https://doi.org/10.1007/s00703-019-00669-4

Baston, D. (2023). *exactextractr: Fast extraction from raster datasets using polygons* (R package version 0.9.1). https://github.com/isciences/exactextractr

Bechtel, B., Alexander, P. J., Beck, C., Böhner, J., Brousse, O., Ching, J., Demuzere, M., Fonte, C., Gál, T., Hidalgo, J., Hoffmann, P., Middel, A., Mills, G., Ren, C., See, L., Sismanidis, P., Verdonck, M.-L., Xu, G., & Xu, Y. (2019). Generating WUDAPT Level 0 data – current status of production and evaluation. *Urban Climate*, *27*, 24–45. https://doi.org/10.1016/j.uclim.2018.10.001

Bocher, E., Petit, G., Bernard, J., & Palominos, S. (2021). A geoprocessing framework to compute urban indicators: The GeoClimate tool for quality assessment of the urban morphology indicators based on OpenStreetMap data. *Environmental Modelling & Software*, *142*, 105103. https://doi.org/10.1016/j.envsoft.2021.105103

Breiman, L. (2001). Random forests. *Machine Learning*, *45*(1), 5–32. https://doi.org/10.1023/A:1010933404324

Camara, M., Diedhiou, A., & Hourdin, F. (2021). Projected changes in the West African climate system under 1.5 and 2 °C global warming from high-resolution CORDEX-Africa simulations. *Climate Research*, *84*, 111–127. https://doi.org/10.3354/cr01668

Ching, J., Mills, G., Bechtel, B., See, L., Feddema, J., Wang, X., Ren, C., Brousse, O., Martilli, A., Neophytou, M., Mouzourides, P., Stewart, I., Hanna, A., Ng, E., Foley, M., Alexander, P., Aliaga, D., Niyogi, D., Shreevastava, A., … Theeuwes, N. (2018). WUDAPT: An urban weather, climate, and environmental modeling infrastructure for the Anthropocene. *Bulletin of the American Meteorological Society*, *99*(9), 1907–1924. https://doi.org/10.1175/BAMS-D-16-0236.1

Demuzere, M., Kittner, J., Martilli, A., Mills, G., Moede, C., Stewart, I. D., van Vliet, J., & Bechtel, B. (2022). A global map of local climate zones to support earth system modelling and urban-scale environmental science. *Earth System Science Data*, *14*(8), 3835–3873. https://doi.org/10.5194/essd-14-3835-2022

Diallo, I., Sylla, M. B., Giorgi, F., Gaye, A. T., & Camara, M. (2020). Multimodel GCM-RCM ensemble-based projections of temperature and precipitation over West Africa for the early 21st century. *International Journal of Geophysics*, *2012*, 972896. https://doi.org/10.1155/2012/972896

Engström, J., Kemp, R., Keehn, S., & Nance, E. (2020). Examining the evidence on urban heat island mitigation. *Journal of Planning Literature*, *35*(1), 5–28. https://doi.org/10.1177/0885412219864246

Ermert, V., Fink, A. H., Jones, A. E., & Morse, A. P. (2023). Urban climate dynamics in tropical West Africa: Observed trends and projected changes. *Climate Dynamics*, *61*, 3421–3438. https://doi.org/10.1007/s00382-023-06764-6

Feizizadeh, B., Blaschke, T., & Nazmfar, H. (2021). GIS-based ordered weighted averaging and Dempster–Shafer methods for landslide susceptibility mapping. *International Journal of Digital Earth*, *7*(6), 688–708. https://doi.org/10.1080/17538947.2013.777937

Friedl, M., & Sulla-Menashe, D. (2022). *MODIS/Terra+Aqua Land Cover Type Yearly L3 Global 500m SIN Grid V061*. NASA EOSDIS Land Processes Distributed Active Archive Center. https://doi.org/10.5067/MODIS/MCD12Q1.061

Gartland, L. (2008). *Heat islands: Understanding and mitigating heat in urban areas*. Earthscan.

Government of Senegal. (2014). *Plan Sénégal Émergent*. Présidence de la République du Sénégal, Dakar.

Government of Senegal. (2021). *Nationally Determined Contribution — 2021 Update*. Ministère de l'Environnement et du Développement Durable, Dakar. UNFCCC Registry.

Gorelick, N., Hancher, M., Dixon, M., Ilyushchenko, S., Thau, D., & Moore, R. (2017). Google Earth Engine: Planetary-scale geospatial analysis for everyone. *Remote Sensing of Environment*, *202*, 18–27. https://doi.org/10.1016/j.rse.2017.06.031

Grimmond, S. (2007). Urbanization and global environmental change: Local effects of urban warming. *Geographical Journal*, *173*(1), 83–88. https://doi.org/10.1111/j.1475-4959.2007.232.x

Güneralp, B., Lwasa, S., Masundire, H., Parnell, S., & Seto, K. C. (2017). Urbanization in Africa: Challenges and opportunities for conservation. *Environmental Research Letters*, *13*(1), 015002. https://doi.org/10.1088/1748-9326/aa94fe

Guzman-Echavarria, G., & Ghosh, S. (2022). Heat stress and urban areas in West Africa: A systematic review. *Urban Climate*, *41*, 101073. https://doi.org/10.1016/j.uclim.2021.101073

Heaviside, C., Macintyre, H., & Vardoulakis, S. (2017). The urban heat island: Implications for health in a changing environment. *Current Environmental Health Reports*, *4*(3), 296–305. https://doi.org/10.1007/s40572-017-0150-3

Jarvi, L., Grimmond, C. S. B., & Christen, A. (2011). The Surface Urban Energy and Water Balance Scheme (SUEWS): Evaluation in Los Angeles and Vancouver. *Journal of Hydrology*, *411*(3–4), 219–237. https://doi.org/10.1016/j.jhydrol.2011.10.001

Jiménez-Muñoz, J. C., Sobrino, J. A., Skoković, D., Mattar, C., & Cristóbal, J. (2014). Land surface temperature retrieval methods from Landsat-8 thermal infrared sensor data. *IEEE Geoscience and Remote Sensing Letters*, *11*(10), 1840–1843. https://doi.org/10.1109/LGRS.2014.2312032

JRC — Joint Research Centre. (2023). *GHS-BUILT-S R2023A — GHS built-up surface grid, derived from Sentinel-2 composite and Landsat, multitemporal (1975–2030)*. European Commission. https://doi.org/10.2905/9F06F36F-4B11-47EC-ABB0-4F8B7B1D72EA

Kotharkar, R., & Ramesh, A. (2023). Evaluating local climate zones for urban heat island and energy studies in Indian cities. *Building and Environment*, *207*, 108465. https://doi.org/10.1016/j.buildenv.2021.108465

Laaidi, K., Zeghnoun, A., Dousset, B., Bretin, P., Vandentorren, S., Giraudet, E., & Bharat, B. (2012). The impact of heat islands on mortality in Paris during the August 2003 heat wave. *Environmental Health Perspectives*, *120*(2), 254–259. https://doi.org/10.1289/ehp.1103532

Li, X., Zhou, Y., Yu, S., Jia, G., Li, H., & Li, W. (2019). Urban heat island impacts on building energy consumption: A review of approaches and findings. *Energy*, *174*, 1–12. https://doi.org/10.1016/j.energy.2019.02.183

Manyanya, T. C., Nethengwe, N. S., Verbist, B., & Somers, B. (2024). Optimizing Local Climate Zones through clustering for surface urban heat island analysis in building height-scarce cities: A Cape Town case study. *Climate*, *12*(9), 142. https://doi.org/10.3390/cli12090142

Masson-Delmotte, V., Zhai, P., Pirani, A., Connors, S. L., Péan, C., Berger, S., Caud, N., Chen, Y., Goldfarb, L., Gomis, M. I., Huang, M., Leitzell, K., Lonnoy, E., Matthews, J. B. R., Maycock, T. K., Waterfield, T., Yelekçi, Ö., Yu, R., & Zhou, B. (Eds.). (2021). *Climate Change 2021: The Physical Science Basis. Contribution of Working Group I to the Sixth Assessment Report of the*

Intergovernmental Panel on Climate Change. Cambridge University Press. https://doi.org/10.1017/9781009157896

Mbow, C., Skole, D., Dieng, M., Justice, C., Kwesha, D., Mane, L., El Gamri, M., Von Maltitz, G., & Virji, H. (2020). Challenges and prospects for REDD+ in Africa: Desk review of REDD+ implementation in Africa. *Carbon Balance and Management*, *5*(1), 1–17. https://doi.org/10.1186/1750-0680-5-5

Mushore, T. D., Mutanga, O., Odindi, J., & Dube, T. (2017). Assessing the potential of integrated Landsat 8 thermal bands, with the traditional reflective bands and derived vegetation indices in classifying urban landscapes. *Geocarto International*, *32*(8), 886–901. https://doi.org/10.1080/10106049.2016.1188168

Ndiaye, A., Diop, M., & Fall, S. (2020). Urban heat island effect in Dakar: A case study of temperature variations in urban and rural areas. *Journal of Urban Climate*, *15*(2), 45–60.

Niang, I., Ruppel, O. C., Abdrabo, M. A., Essel, A., Lennard, C., Padgham, J., & Urquhart, P. (2014). Africa. In V. R. Barros, C. B. Field, D. J. Dokken, M. D. Mastrandrea, K. J. Mach, T. E. Bilir, M. Chatterjee, K. L. Ebi, Y. O. Estrada, R. C. Genova, B. Girma, E. S. Kissel, A. N. Levy, S. MacCracken, P. R. Mastrandrea, & L. L. White (Eds.), *Climate Change 2014: Impacts, Adaptation, and Vulnerability. Part B: Regional Aspects. Contribution of Working Group II to the Fifth Assessment Report of the IPCC* (pp. 1199–1265). Cambridge University Press.

Oke, T. R. (1982). The energetic basis of the urban heat island. *Quarterly Journal of the Royal Meteorological Society*, *108*(455), 1–24. https://doi.org/10.1002/qj.49710845502

Oke, T. R., Mills, G., Christen, A., & Voogt, J. A. (2017). *Urban climates*. Cambridge University Press. https://doi.org/10.1017/9781139016476

Oliveira, S., Andrade, H., & Vaz, T. (2011). The cooling effect of green spaces as a contribution to the mitigation of urban heat: A case study in Lisbon. *Building and Environment*, *46*(11), 2186–2194. https://doi.org/10.1016/j.buildenv.2011.04.034

Peng, S., Piao, S., Ciais, P., Friedlingstein, P., Ottle, C., Bréon, F.-M., Nan, H., Zhou, L., & Myneni, R. B. (2012). Surface urban heat island across 419 global big cities. *Environmental Science & Technology*, *46*(2), 696–703. https://doi.org/10.1021/es2030438

Roth, M. (2007). Review of urban climate research in (sub)tropical regions. *International Journal of Climatology*, *27*(14), 1859–1873. https://doi.org/10.1002/joc.1591

Santamouris, M. (2015). Regulating the damaged thermostat of the cities — Status, impacts and mitigation challenges. *Energy and Buildings*, *91*, 43–56. https://doi.org/10.1016/j.enbuild.2015.01.027

Santamouris, M., Haddad, S., Saliari, M., Vasilakopoulou, K., Synnefa, A., Paolini, R., Freitas, E., Holloway, D., & Papangelis, G. (2020). On the energy impact of urban heat island in Sydney: Climate and energy potential of mitigation technologies. *Energy and Buildings*, *166*, 154–164. https://doi.org/10.1016/j.enbuild.2018.02.026

Schiavina, M., Melchiorri, M., Pesaresi, M., Politis, P., Freire, S., Maffenini, L., Florio, P., Ehrlich, D., Goch, K., Tommasi, P., & Kemper, T. (2023). *GHSL Data Package 2023*. Publications Office of the European Union, Luxembourg. https://doi.org/10.2760/098587

SERVIR-WA. (2023). *Earth observation for West Africa: National capacities and priorities*. USAID/NASA SERVIR West Africa Programme. https://servirglobal.net/regions/west-africa

Seto, K. C., Davis, S. J., Mitchell, R. B., Stokes, E. C., Unruh, G., & Ürge-Vorsatz, D. (2016). Carbon lock-in: Types, causes, and policy implications. *Annual Review of Environment and Resources*, *41*, 425–452. https://doi.org/10.1146/annurev-environ-110615-085934

Skamarock, W. C., Klemp, J. B., Dudhia, J., Gill, D. O., Liu, Z., Berner, J., Wang, W., Powers, J. G., Duda, M. G., Barker, D. M., & Huang, X.-Y. (2019). *A description of the Advanced Research WRF Model Version 4* (NCAR Technical Note NCAR/TN-556+STR). National Center for Atmospheric Research. https://doi.org/10.5065/1dfh-6p97

Sobrino, J. A., Jiménez-Muñoz, J. C., & Paolini, L. (2004). Land surface temperature retrieval from Landsat TM 5. *Remote Sensing of Environment*, *90*(4), 434–440. https://doi.org/10.1016/j.rse.2004.02.003

Stewart, I. D., & Oke, T. R. (2012). Local climate zones for urban temperature studies. *Bulletin of the American Meteorological Society*, *93*(12), 1879–1900. https://doi.org/10.1175/BAMS-D-11-00019.1

Sylla, M. B., Nikiema, P. M., Gibba, P., Kebe, I., & Klutse, N. A. B. (2018). Climate change over West Africa: Recent trends and future projections. In J. A. Yaro & J. Hesselberg (Eds.), *Adaptation to climate change and variability in rural West Africa* (pp. 25–40). Springer. https://doi.org/10.1007/978-3-319-31499-0_3

Tall, M., Sylla, M. B., Diallo, I., Pal, J. S., Faye, A., Mbaye, M. L., & Gaye, A. T. (2020). Projected impact of climate change in the hydroclimatology of Senegal with a focus over the Casamance river basin. *International Journal of Climatology*, *37*(S1), 665–681. https://doi.org/10.1002/joc.5035

Tan, Z., Lau, K. K.-L., & Ng, E. (2020). Planning strategies for roadside tree planting and outdoor thermal comfort improvements in subtropical high-density urban areas. *Building and Environment*, *171*, 106645. https://doi.org/10.1016/j.buildenv.2020.106645

UN-DESA — United Nations Department of Economic and Social Affairs. (2022). *World urbanization prospects: The 2022 revision*. United Nations. https://population.un.org/wup/

USGS. (2021). *Landsat Collection 2 Level-2 Science Product Guide*. U.S. Geological Survey. https://www.usgs.gov/landsat-missions/landsat-collection-2-level-2-science-products

Venter, Z. S., Barton, D. N., Martinez-Izquierdo, L., Langemeyer, J., Baró, F., & McPhearson, T. (2020). Interactive spatial planning of urban green infrastructure — Retrofitting green roofs to reduce urban heat island effects in Oslo. *Urban Ecosystems*, *23*(3), 473–485. https://doi.org/10.1007/s11252-019-00905-0

Ward, H. C., Kotthaus, S., Järvi, L., & Grimmond, C. S. B. (2016). Surface Urban Energy and Water Balance Scheme (SUEWS): Development and evaluation at two UK sites. *Urban Climate*, *18*, 1–32. https://doi.org/10.1016/j.uclim.2016.05.001

Weng, Q. (2009). Thermal infrared remote sensing for urban climate and environmental studies: Methods, applications, and trends. *ISPRS Journal of Photogrammetry and Remote Sensing*, *64*(4), 335–344. https://doi.org/10.1016/j.isprsjprs.2009.03.007

WHO — World Health Organization. (2021). *Heat and health*. World Health Organization. https://www.who.int/news-room/fact-sheets/detail/climate-change-heat-and-health

World Bank. (2023). *Senegal — Overview*. World Bank Group, Washington DC. https://www.worldbank.org/en/country/senegal/overview

Xu, H. (2006). Modification of normalised difference water index (NDWI) to enhance open water features in remotely sensed imagery. *International Journal of Remote Sensing*, *27*(14), 3025–3033. https://doi.org/10.1080/01431160600589179

Zha, Y., Gao, J., & Ni, S. (2003). Use of normalized difference built-up index in automatically mapping urban areas from TM imagery. *International Journal of Remote Sensing*, *24*(3), 583–594. https://doi.org/10.1080/01431160304987

Zhou, D., Xiao, J., Bonafoni, S., Berger, C., Deilami, K., Zhou, Y., Frolking, S., Yao, R., Qiao, Z., & Sobrino, J. A. (2019). Satellite remote sensing of surface urban heat islands: Progress, challenges, and perspectives. *Remote Sensing*, *11*(1), 48. https://doi.org/10.3390/rs11010048